Modelling and Simulation in Materials Science and Engineering

**PAPER** • **OPEN ACCESS**

# Dislocation structure analysis in the strain gradient of torsion loading: a comparison between modelling and experiment

To cite this article: Markus Stricker *et al* 2022 *Modelling Simul. Mater. Sci. Eng.* **30** 035007





OPEN ACCESS
IOP Publishing
Modelling and Simulation in Materials Science and Engineering
Modelling Simul. Mater. Sci. Eng. **30** (2022) 035007 (22pp) https://doi.org/10.1088/1361-651X/ac4d77

# Dislocation structure analysis in the strain gradient of torsion loading: a comparison between modelling and experiment

**Markus Stricker[1,2,*], Michael Ziemann[3], Mario Walter[3], Sabine M Weygand[4], Patric Gruber[3] and Daniel Weygand[2]**

[1] Interdisciplinary Centre for Advanced Materials Simulation, Ruhr-University Bochum, Universitätsstraße 150, 44801 Bochum, Germany
[2] Institute for Applied Materials (IAM-ZM), Karlsruhe Institute of Technology, Kaiserstraße 12, 76131 Karlsruhe, Germany
[3] Institute for Applied Materials (IAM-MMI), Karlsruhe Institute of Technology, Herrmann-von-Helmholtz-Platz 1, 76344 Eggenstein-Leopoldshafen, Germany
[4] Faculty of Mechanical Engineering and Mechatronics (MMT), Karlsruhe University of Applied Sciences, Moltkestraße 30, 76133 Karlsruhe, Germany

E-mail: markus.stricker@rub.de

Received 16 September 2021, revised 13 January 2022
Accepted for publication 20 January 2022
Published 8 February 2022

**Abstract**

Complex stress states due to torsion lead to dislocation structures characteristic for the chosen torsion axis. The formation mechanism of these structures and the link to the overall plastic deformation are unclear. Experiments allow the analysis of cross sections only ex situ or are limited in spacial resolution which prohibits the identification of the substructures which form within the volume. Discrete dislocation dynamics simulations give full access to the dislocation structure and their evolution in time. By combining both approaches and comparing similar measures the dislocation structure formation in torsion loading of micro wires is explained. For the ⟨100⟩ torsion axis, slip traces spanning the entire sample in both simulation and experiment are observed. They are caused by collective motion of dislocations on adjacent slip planes. Thus these slip traces are not atomically sharp. Torsion loading around a ⟨111⟩ axis favors plasticity on the primary slip planes perpendicular to the torsion axis and dislocation storage through cross-slip and subsequent collinear junction

*Author to whom any correspondence should be addressed.

formation. Resulting hexagonal dislocation networks patches are small angle grain boundaries. Both, experiments and discrete dislocation simulations show that dislocations cross the neutral fiber. This feature is discussed in light of the limits of continuum descriptions of plasticity.

Keywords: strain gradient, discrete dislocation dynamics, microwire torsion, misorientation

(Some figures may appear in colour only in the online journal)

## 1. Introduction

Mechanical properties of small scale metallic structures have been investigated in detail focusing on the size effect [1–4]. For larger structures under complex loading conditions a direct link between dislocation structures and mechanical properties as well as experimental analysis of those structures remains challenging [5–8]. For example, the dislocation structure forming in twisted nano- and microwires and its connection to the mechanical properties as well as deformation mechanisms is not yet clear: torsion experiments on thin metallic wires [9] triggered the development of a complex strain gradient model in order to describe the size dependency of the mechanical response of polycrystalline wires under torsion. Molecular dynamics (MD) and discrete dislocation dynamics (DDD) simulations of cyclically twisted single-crystalline thin wires reveal a strong dependence on the crystallographic orientation [10–15]. Continuum dislocation dynamics (CDD) investigations show dislocation density distributions within the wire consistent with DDD simulations [12, 16, 31] under torsion. A recent combined MD and DDD investigation show the development of dislocation networks in the limit of very low dislocation densities [17]. Homogeneous deformation in face centered cubic (fcc) crystals for a $\langle 110 \rangle$ torsion axis and heterogeneous deformation for $\langle 100 \rangle$ and $\langle 111 \rangle$ with localization at the forming twist boundaries are found as the governing deformation mechanisms [10, 11]. Due to the small diameters and high loading rate of the wires in MD simulations, dislocations are nucleated at free surfaces. A larger sample diameter changes the mechanism.

In micrometer-sized specimen under uniaxial and cyclic loading the emergence of complex dislocation networks is observed. Depending on the orientation and loading amplitude, different dislocation pile-ups are generated around the center of the sample, which can be interpreted as small angle grain boundaries [12]. Due to the large number of dislocations and therefore increased number of stable junctions, a large fraction of the pile-up like structures in the interior are rather stable and persist—with some relaxation—even after unloading. These pile-up like structures can also consist of dislocations on parallel slip planes [16].

Experimental studies on microwires in torsion loading focus mainly on the size effect and the underlying competing mechanisms of its origin [7, 18–20]. More recently, the investigation of the mechanical behavior of alternating single-crystalline—so called *bamboo structured*—wires under torsion loading were reported [8]. Only the global mechanical response is measured in these experiments due to the experimental setup. But the distribution of plasticity is quite non-uniform along the wire with an aspect ratio of approximately 500 and consisting of alternating $\langle 100 \rangle$ and $\langle 111 \rangle$ oriented grains with respect to the torsion axis.

Therefore, as a follow up to reference [8], we focus on a detailed investigation of the dislocation structure forming in twisted single crystalline micrometer-sized fcc wires using DDD. Both $\langle 100 \rangle$ and $\langle 111 \rangle$ torsion axes are considered. The combination of DDD for the evolution of the microstructure and specifically tailored experiments for a grain based comparison of plastic slip allow the analysis of the formation of the dislocation network, topological changes,

and the deformation mechanisms leading to the observed structures and surface traces of dislocations leaving the sample. There is no direct method to access the structure and evolution of a dislocation network experimentally *in situ*. Therefore, indirect ex situ measurements based on the distortions of the lattice due to the presence of dislocations are used: the fusion of experimental and simulation data is established based the common language of *misorientations*. The experimental examples are analyzed by high resolution electron backscatter diffraction (EBSD), exceeding the spatial resolution of the Laue diffraction approach [8] before. Simulation results are postprocessed to provide local misorientation information as described in appendix A.1.

The paper is organized as follows. In section 2 we first present the DDD framework including the used parameters as well as experimental details. Section 3 shows simulation results, postprocessing and the experimental observations. These are then discussed in section 4, including some remarks on averaging aspects for the equivalent plastic strain which provides a link for comparison to continuum plasticity descriptions. The study is then concluded in section 5.

## 2. Methods

This work focuses on the plastic deformation behavior of fcc metals under torsion. The microwires in the experiments are gold because such wires are available commercially and oxidation is limited. DDD simulations use parameters for elastically isotropic aluminum. The focus of the observations is on the evolution and development of the dislocation structure. Only indirect measures like local misorientations are compared. These are independent of the lattice parameter and elastic constants and provide a common language for comparison. Hence, the underlying *material* is of less importance in this context. The most important property is the crystal structure (fcc), since it provides the plastic degrees of freedom (dof), which are the basis for the observed dislocation structure. A possible influence on the results regarding the chosen material (or material model) is discussed in section 4.

### *2.1. Discrete dislocation dynamics*

A DDD framework is used to follow the dislocation structure evolution during loading. The framework allows modeling finite sized samples in three dimensions for small strains and solving the complete boundary value problem. It is described in detail elsewhere [12, 21–23] and only a short description is given here.

Dislocations are discretized by nodes connected by piecewise straight segments. Their motion is calculated according to the resolved Peach–Koehler force acting along the segments in their slip plane. Finiteness of the sample is implemented via the superposition principle, which accounts for both the boundary conditions and image forces [22, 24]. Changes in the dislocation topology like junction formation, cross-slip and annihilation are treated with constitutive rules [22, 25]. Material parameters for fcc isotropic aluminum are used as a model system (shear modulus $G = 27$ GPa, Poisson's ratio $\nu = 0.347$, lattice parameter $a = 0.404$ nm).

The computational cost of DDD simulations does not allow for the same sample dimensions and strain levels compared to those of the experiments [26]. Therefore a simplified and smaller sample geometry is taken. In the present study, the global mechanical response in terms of normalized moment versus surface shear strain is not of interest for two reasons: (i) this information is experimentally not accessible as only an integrated value of all grains in a wire can be measured; (ii) there is not a universal or unique behavior of single similarly oriented crystal

sections due to the influence of neighboring grains. Therefore instead of modeling the alternating structure of $\langle 100 \rangle$ and $\langle 111 \rangle$ oriented grains, individual grains with the two orientations are subjected to torsion boundary conditions. The DDD samples have a square cross section as opposed to the circular cross section of the experimental wires, which allows the usage of an efficient finite element solver [26]. The choice of this efficient solver also restricts the used DDD code to cuboid sample shapes. Due to the square geometry, zones of lower shear stresses w.r.t. a circular cross-section are present towards the corners, but the dislocation behavior in the inscribed cylinder of the sample is not fundamentally altered, e.g. the shear stress gradient occurring under torsion on each slip system is present and only distorted. The choice can further be justified by comparison to published MD and DDD simulations of $\langle 100 \rangle$ and $\langle 111 \rangle$ circular cross sections which show a similar planar dislocation arrangement [10, 11, 16]. I.e. our observed dislocation structures match the results in the presented references despite different cross-sectional geometries.

The initial dislocation structure consists of randomly distributed Frank–Read sources (w.r.t. position and orientation) in a cylindrical subvolume of the cuboid shape. This is done to further avoid activation of sources towards the corners outside the cylindrical subvolume. The initial dislocation density on each slip system is $\approx 4.2 \times 10^{11}$ m$^{-2}$, resulting in a total density of approximately $\rho_{\text{start}} \approx 5 \times 10^{12}$ m$^{-2}$. The source length is chosen to be $1.5/\sqrt{\rho_{\text{start}}}$ with a variation of $\pm 20\%$. The choice for the initial spatial dislocation distribution places the sample in a multiplication controlled regime [12]. A higher density is chosen in the simulations as compared to the well annealed samples in the experiments to retain the important features of the dislocation structure: smaller samples with a higher density behave *equivalent* to larger samples with a lower density in accordance with the similitude principle [27].

The torsion loading of the sample is applied through boundary conditions on the surface nodes of the wire-like shape: (i) the nodes belonging to the bottom surface are fixed; (ii) the side faces have traction free boundary conditions; (iii) the top surface nodes have mixed conditions: the out-of-plane dof are set to be traction free, while the in-plane dof have prescribed displacements corresponding to the imposed torsion angle. These boundary conditions allow for the development of waviness of the top surface under torsion loading of wires with a square cross section. Both the waviness and the square cross section introduce spurious stress fields at the top and the corners respectively. Suppressing the waviness on both ends would introduce additional spurious stress components. Applying traction free condition in the normal direction of the top surfaces is a *softer* boundary constraint. This surface corresponds to one grain boundary in the bamboo structure which is also not a rigid interface.

By rotating the crystal orientation with respect to the torsion axes we checked that the fundamental observations reported later remain valid and are not artifacts of the square shape of the cross section. Furthermore the detailed analysis is limited to a cylindrical subvolume with the cylinder axis coinciding with the torsion axis. The radius of the cylinder is taken as half the side length of the square cross section thereby excluding the corners in the analysis. Additionally, the resolved shear stresses acting on each slip system have been analyzed. In case of a cylindrical cross section for a given slip system the corresponding shear stress varies linearly within the cross section of the slip plane and the neutral line of zero shear stress intersects the torsion axis. In case of a square cross section, the corresponding shear stress distribution is similar within the cylindrical subvolume: there is a neutral line crossing the torsion axis and a modulated gradient perpendicular to the neutral line. The zone of maximal differences are towards the corners of the square, which are excluded from averages shown later. Corresponding shear stress distributions have been analyzed in [12, 14]. In [14] the final dislocation pile-ups originate from a single source located close to the surface under torsion load indicate moderately distorted equal stress lines in the slip plane. With decreasing distance from the

torsion axis the resolved shear stress distribution per slip system in the square cross section approaches the one found in cylindrical geometries. As the overall shear stress characteristics on each slip system is similar for cylindrical and square cross sections within the analyzed cylindrical subvolume the plasticity by dislocation glide around the torsion axis is expected to be qualitatively identical.

The displacements during loading are imposed with a torsion angular rate of $\dot{\phi} = 1.7^\circ\ \mu s^{-1}$ (this translates into a surface strain rate of $7.4 \times 10^3\ s^{-1}$) like in [12], where it was found that the influence of different torsion rates on the overall response is not significant. In the $\langle 100 \rangle$ oriented sample, the cubic axes of the crystal are parallel to the laboratory frame. For the sample with torsion axis parallel to $\langle 111 \rangle$ one Burgers vector in the plane orthogonal to the torsion axis is aligned with an axis of the lab frame. Variations of rotations around the torsion axes have also been checked on smaller samples and no significant dependence of the relevant measures was found.

Dislocation structures are analyzed in the loaded state, for technical details the reader is referred to appendix A. This is in contrast to the experimental cross-sections, where the analysis is only possible ex situ in the unloaded state. The influence of loaded vs unloaded states in simulations was investigated by unloading smaller samples with a side length of 2 $\mu$m with otherwise identical boundary conditions. These were then subjected to the same analysis before and after relaxation. We found that while the dislocation structure rearranged during unloading, the qualitative outcome did not change with unloading. That is, the measured signatures of developed dislocation structures are qualitatively equivalent before and after unloading. As expected, the main differences occur towards the corners of the square cross-section. The dislocation rearrangement during unloading is assumed to be negligible for the larger samples, due to the larger number of dislocations present leading to a larger number of possible pinning sites, which stabilize the dislocation structure. The nature of the simulation vs experiment comparison is qualitative due to both the sample size difference and differences in boundary conditions: single crystals vs bamboo structured wires. Based on the remarks above we compare results of the larger simulations analyzed in the loaded state to experiments instead of unloaded smaller ones.

### *2.2. Experimental sample preparation and microstructure*

The base material for the experiments is high purity gold (99.99 at%, supplier Heraeus Group, Germany) in the form of polycrystalline wires. Using gold as reference material offers several advantages: the fcc-structured pure noble metal in the form of micro wires is commercially available within a wide range of different diameters, ranging from 5 $\mu$m to several 100 $\mu$m. Using gold circumvents the issue of the formation of oxide layers at the surface during heat treatment, which might affect the mechanical behavior of a specimen and lower the accuracy of diffraction investigations. We use wires with a diameter of 25 $\mu$m. A minimum length of some deca mm is necessary for the testing procedure [7]. Wires with single crystalline cross sections, a so called *bamboo structure* [8], are used since it is not possible to produce single crystalline specimens in these dimensions. These samples are produced by heat treating the supplied polycrystalline micro wires at 800 °C for about 170 h in a high vacuum glass tube furnace.

The wires are then twisted up to a defined plastic shear strain at the surface of $\gamma_{\mathrm{pl,r=R}} = 2.5\%$, with an in-house developed micro torsion device [28, 29]. The chosen degree of deformation is an integral value related to the entire gauge length of the wire. The resulting torsion moment $M_\mathrm{t}$ for a given load is identical in every cross section of the sample. But due to the

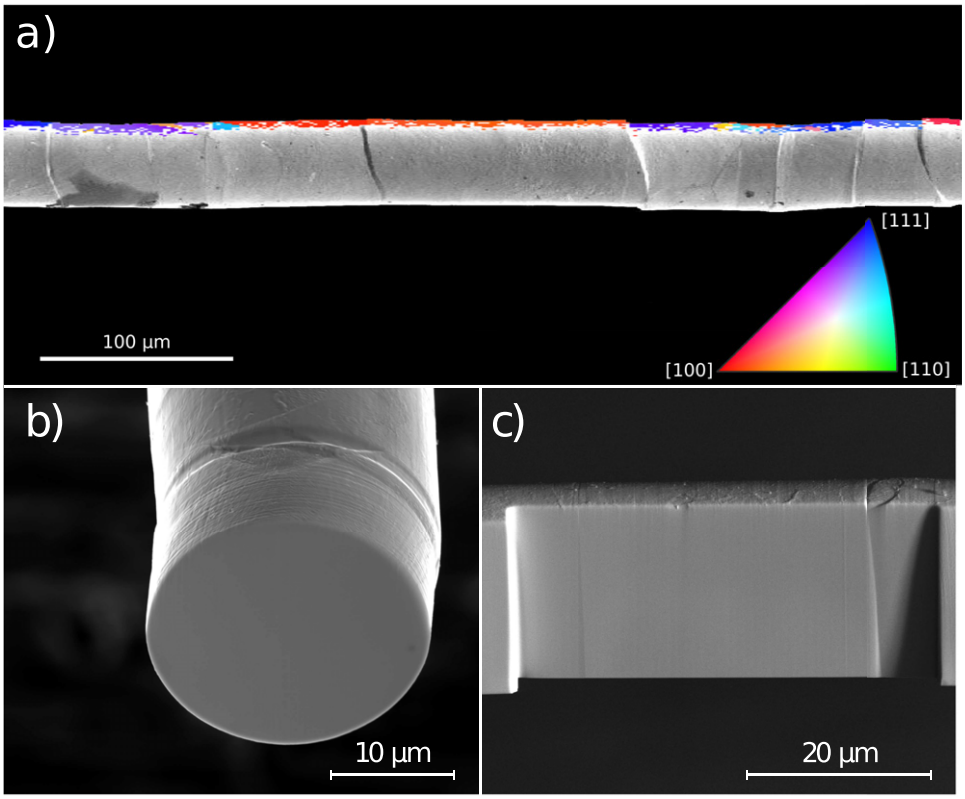


**Figure 1.** SEM micrographs: (a) bamboo structured Au-wire (alternating ⟨111⟩ and ⟨100⟩ grains), (b) cross section and (c) longitudinal section of the wire prepared by FIB milling.

bamboo structure the resulting deformation within individual grains is affected by the individual misalignment between the crystals orientation and the wire and experimental axis.

After loading, several segments of the wire are glued on scanning electron microscope (SEM) stubs with silver paint. The stubs are mounted into a dual beam SEM-focused ion beam (FIB) microscope (FEI NanoLab 200), equipped with an EBSD system from Oxford Instruments. The recorded Kikuchi patterns are analyzed using the high resolution EBSD (HREBSD) tool CrossCourt 3 (BLG Productions Ltd) [30]. In a first step EBSD surface scans along the samples are performed to determine the orientation of individual grains related to the wires main axis (cf figure 1(a)). In a second step, twin free, ⟨100⟩ and ⟨111⟩ oriented grains with respect to the torsion axis and a minimum length of 30 $\mu$m are selected. Some of them are cut by FIB perpendicular to the torsion axis between the two grain boundaries (figure 1(b)). Others are centrically cut along the torsion axis direction (figure 1(c)). This procedure is destructive. The following data from experiments is therefore not from one grain but a compilation of data sets from different grains with the same orientation parallel to the torsion axis. To identify macroscopic and microscopic orientation gradients resulting from deformation, the cross- and longitudinal-sections are EBSD-scanned with a step size of 100–300 nm depending on the degree of perturbing charging effects with decreasing step size.

## 3. Results

In the following section we present results of the local deformation in form of misorientations and plastic strain distributions. These results are used to calculate kernel average misorientation (KAM) or related selective misorientation measures. KAM and selective misorientation measures reveal local dislocation structures. We further present details of the 3D dislocation structure from the DDD simulations which are not accessible with the other methods.

### *3.1. DDD misorientation maps, microstructure and plastic strain*

The misorientation angle $\theta$ is calculated from the displacement fields of the dislocations including boundary corrections fields. For details of the calculation the reader is referred to appendix A.1.

Figure 2(a) depicts a snapshot of the dislocation network of a sample with a $\langle 100 \rangle$ torsion axis. Figures 2(b)–(d) show misorientations obtained within a cross section containing the torsion axis located at half of the width. Figure 2(b) shows the misorientation with respect to the reference voxel in the center on the bottom of the sample on the torsion axis; figure 2(c) shows the misorientation as a function of the sample height along three lines parallel to the torsion axis located at $1/3$, $1/2$ and $2/3$ width across the section and their average; and figure 2(d) shows the misorientation with respect to the right upper neighbor cell.

With $50\times$ amplified plastic displacements, surface slip traces are visible (figure 2(a)). These are not confined to a single slip plane, but appear in all possible directions of Burgers vectors and multiple times. In figure 2(b) the rotation angle is used for coloring and the arrows indicate the projected rotation axis. Within the cutting plane the local rotation axes are mainly parallel to the torsion axis. Deviations from the parallel structure in the lower part are due to the fixed boundary conditions. In the central and upper part the deviation hints at dislocation structures on the respectively inclined glide planes. The local rotation axes within the cross-section are shown as arrows. The line plots in figure 2(c) show a rather homogeneous gradient of the misorientation in torsion direction. To reveal local changes and regions with high dislocation density, the misorientation with respect to the upper right neighbor is analyzed. The selective misorientation analysis with respect to the upper right neighbor (figure 2(d)) is done to detect regions of large misorientation, which coincide with slip plane intersections of the chosen cutting plane and are a signature of dislocation structures leading to a rotation of the sample around the corresponding glide plane normal. Note that the chosen selective misorientation analysis includes contributions from all present dislocations.

Figures 2(e)–(h) show the same analysis as before but for a sample with a $\langle 111 \rangle$ torsion axis: the amplified plastic displacement of the sample in figure 2(e) shows smaller and less traces due to dislocation slip in the lower part of the sample and some more pronounced traces in the upper part. This is also visible in the misorientation plots (figures 2(f) and (g)) with the reference point in the bottom center: from bottom to top, the misorientation increases in the first third by steps. Local rotation axes are again mainly parallel to the torsion axis. The middle section exhibits very little change in misorientation with height, while in the upper part the misorientation increases again with larger steps, coinciding with the location of surface steps in figure 2(e). In figure 2(h) the selective misorientation with respect to the upper neighbor is shown. Depending on the crystallographic orientation, the selective misorientation measure is chosen either with respect to the upper right or upper neighbor. The surface steps of the two samples show the activity of slip systems. By selection of specific neighbors, such structures are revealed in greater detail compared to the KAM measure.

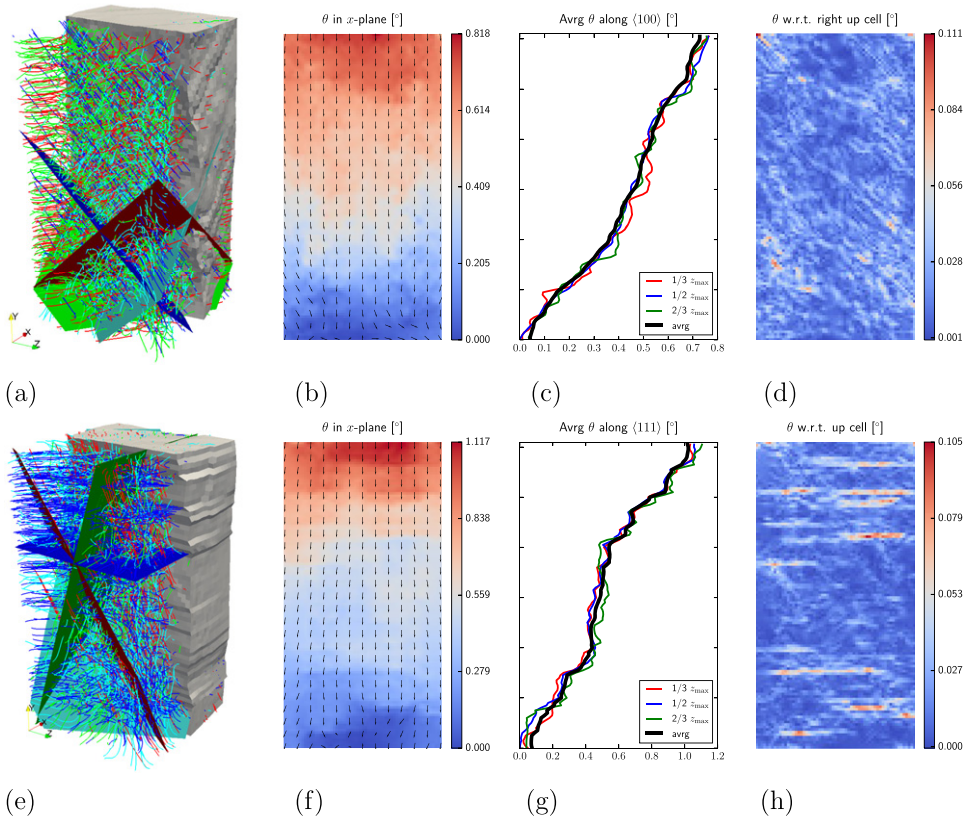


**Figure 2.** DDD simulation results of a sample with an aspect ratio of 2 and total length of 4 $\mu$m. (a)–(d) show a sample with $\langle 100 \rangle$ torsion axis; (e)–(h) with $\langle 111 \rangle$ torsion axis. (a) and (e) show dislocation structures and FEM information. The FEM mesh is cut by a plane with normal parallel to the $x$-axis. The cutting planes contain the torsion axis. Colored planes show orientations of slip plane families. Coloring of dislocations is according to their slip plane normal. In (b) and (f) the misorientation with respect to the reference's point at the bottom center of the cutting plane containing the torsion axis and in (c) and (g) the misorientation along selected lines within the plane are shown. In (d) and (h) the local misorientation with respect to the right upper and the upper neighbor are shown.

Figure 3 shows the dislocation density evolutions during loading. In the $\langle 100 \rangle$ case (figure 3(a)), four slip systems (A3, B4, C3, D4) show a dislocation density increase by one order of magnitude, while all others roughly triple their density. The same grouping of slip systems, albeit much less scatter within each group, is reported in literature for CDD simulation results [31]. The results for the $\langle 111 \rangle$ torsion axis are less clear (figure 3(b)). The dislocation density of slip system (B4) increases by a factor of 16, while the others are scattered from approximately quadrupling (C-systems) to an increase of factor 12 (B2). Note, the B-systems are orthogonal to the torsion axis and show the largest slip activity which leads to the large surface steps shown in figure 2(a).

The contribution of the individual slip systems to the von Mises equivalent plastic strain is shown in figures 3(c) and (d) in the loaded state. Figure 3(c) shows the equivalent plastic strain contributions for the $\langle 100 \rangle$ torsion axis. While not all slip systems contribute equally, three of

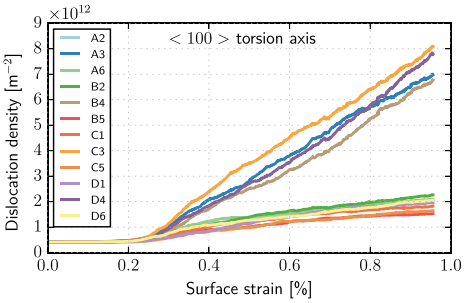


(a) Dislocation density evolution of each slip system for ⟨100⟩ torsion axis.

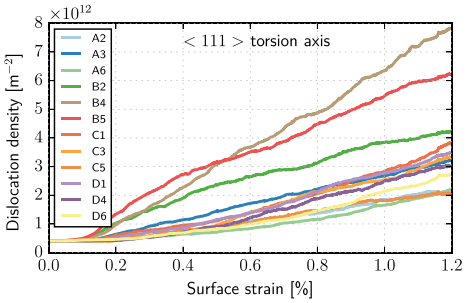


(b) Dislocation density evolution of each slip system for ⟨111⟩ torsion axis. The B-systems are orthogonal to the torsion axis.

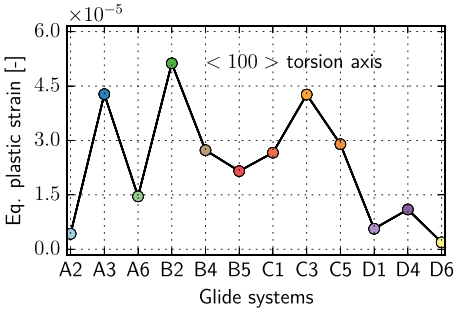


(c) ⟨100⟩ torsion axis.

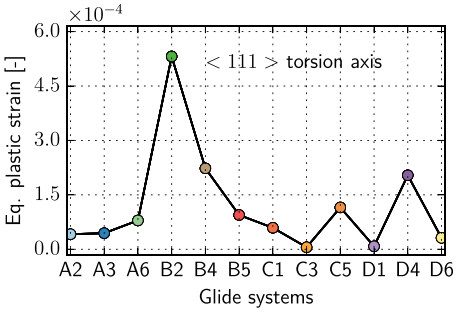


(d) ⟨111⟩ torsion axis. The B-systems are orthogonal to the torsion axis.

**Figure 3.** Dislocation density evolution during torsion and plastic activity of individual slip systems. (a) and (b) show dislocation density evolution vs surface strain. Slip systems are indicated according to Schmid–Boas notation. (c) and (d) Equivalent von Mises plastic strain contributions in the total volume of individual slip systems for both orientations at maximum surface strain. Note that the order of magnitude of the equivalent plastic strain differ for the two torsion axes.

them (A3, B2 and C3) have a substantial contribution. For the ⟨111⟩ torsion axis (figure 3(d)) the values are distributed heterogeneously: most of the equivalent plastic strain originates from slip system B2. The systems B4 and D4 also have a significant contribution, while the others contribute much less.

Figure 4 offers a view of the dislocation structure of a ⟨111⟩ sample within one of the large surface steps indicated by the blue plane. The thickness of the slice corresponds to a voxel height of 66.6 nm used for the evaluation of the misorientations shown in figures 2(e)–(h). The in-plane dislocation structure consists of mostly screw type orientations in a hexagonal network arrangement shown in the center. As expected, the individual hexagons consist of the three Burgers vectors of this slip plane which is shown in the magnified view: different Burgers vectors in the colors red, green and magenta. This picture is representative of such cuts orthogonal to the torsion axis in the ⟨111⟩ cases where the dislocation density of the B-systems is high.

A common trend for both torsion axes is observed for radial averages of the misorientation angles with respect to the center (figure 5). Both show a steep increase close to the center

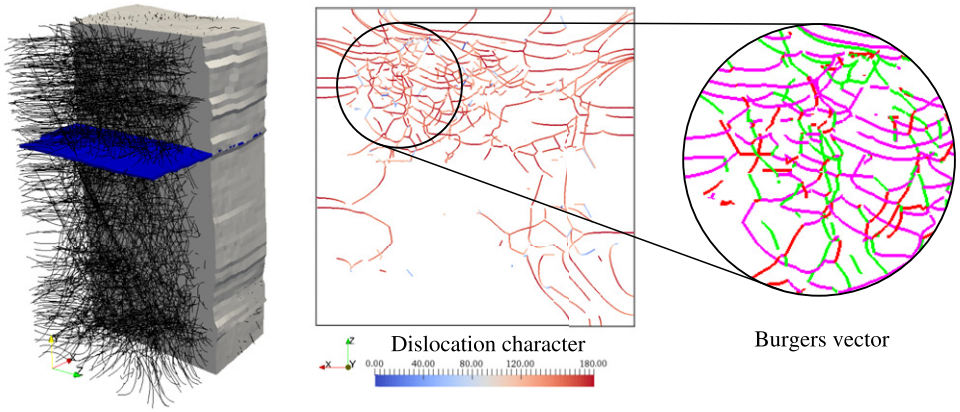


**Figure 4.** Dislocation structure of the ⟨111⟩ sample including a cross section view containing a large surface step indicated by the blue plane. Only dislocations within the blue plane are shown. The indicated plane is a slice of height ≈66 nm. Dislocations arrange in hexagonal network patches of mostly screw orientations (center), each hexagon containing the three Burgers vectors of this plane (right, coloring according to Burgers vector).

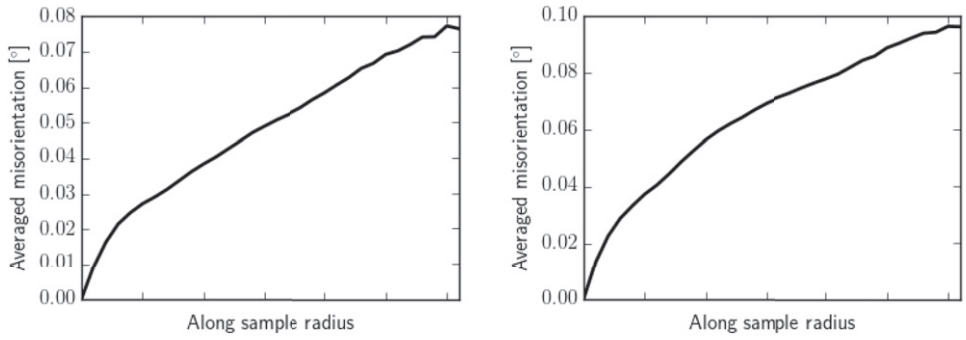


(a) ⟨100⟩ torsion axis. (b) ⟨111⟩ torsion axis.

**Figure 5.** Radially averaged misorientation with respect to center pixel.

and level off slightly towards the outer radius. Averaging is here restricted to the cylindrical subvolume to rule out corner effects on the measures. The difference in magnitude is due to the difference in maximum surface strain of the two simulations.

Figure 6 shows von Mises equivalent plastic strain measures within a cross-section perpendicular to the respective torsion axis employing two different averaging sequences. Figures 6(a) and (d) show the von Mises equivalent plastic strain $\varepsilon_{\mathrm{eq}}\left(\langle\varepsilon_{ij}^{\mathrm{pl}}\rangle\right)$ calculated from the plastic strain tensors averaged over columns of voxels parallel to the torsion axis $\langle\varepsilon_{ij}^{\mathrm{pl}}\rangle$. This homogenizes the plastic deformation along the torsion axis significantly. If this procedure is done in reverse order, i.e. first calculate the von Mises equivalent strain per voxel $\varepsilon_{\mathrm{eq}}(\varepsilon_{ij}^{\mathrm{pl}})$, and then average these values for each column along the torsion axis direction $\langle\varepsilon_{\mathrm{eq}}\rangle$, the local inhomogeneity is retained as depicted in figures 6(b) and (e). Apart from the maximum value a notable difference is found for the equivalent plastic strain at the neutral fiber in the center.

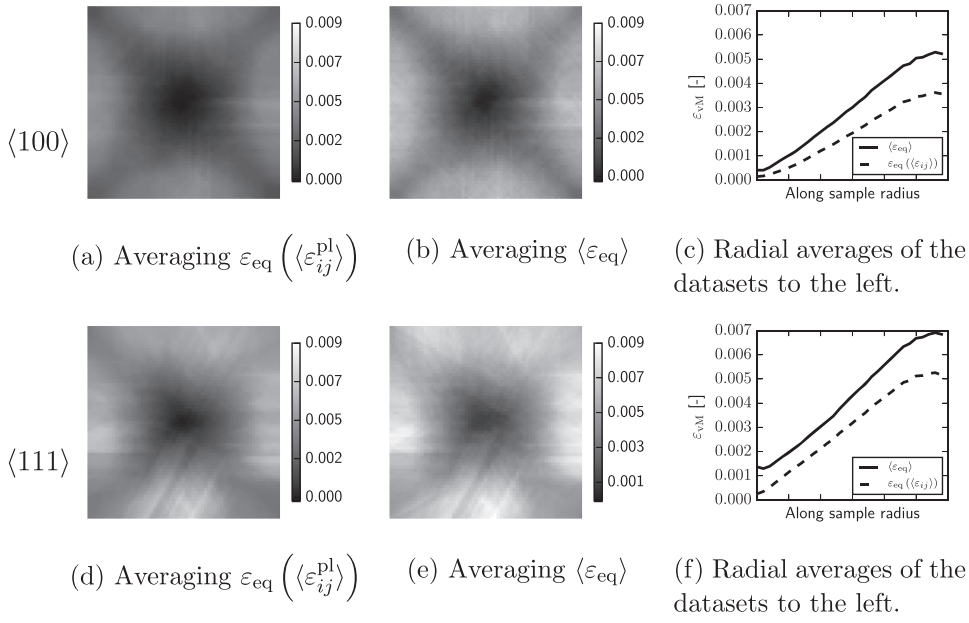


**Figure 6.** Different averages of cross sections from both torsion axes: (a)–(c) show results for ⟨100⟩ torsion axis; (d)–(f) are for the ⟨111⟩ torsion axis. Maps with 61 by 61 elements with local equivalent plastic strains $\varepsilon_{\mathrm{eq}}$ differently averaged over the height of the pillar. (a) and (d) resp. (b) and (e) show the same averaging procedure for both orientations. For details, the reader is referred to the text; (c) and (f) show the radial average comparison of both averaging procedures. The maximum sample radius does not include the corners, but a circle with radius of half the cross section.

Figures 6(c) and (f) show radial averages of the data sets shown in figure 6(a), respective (d), and (b), respective (e). Especially figure 6(f) shows a non-zero plastic strain of the center voxel and its neighbors for the second averaging scheme.

Figure 7 shows selective kernel misorientation angles of the square cross sections of the cross sections. A structure can be identified: lines of high local misorientation angles span across the cross section, indicating the location of dislocation density gradients and therefore possible sites for the formation of small angle twist grain boundaries which accommodate the torsion loading.

### *3.2. Experimental misorientation maps from HREBSD scans*

HREBSD data contains the residual crystal rotation vector components $\omega_x$, $\omega_y$, $\omega_z$ after plastic deformation (twisting). These are appropriately converted and analyzed with the same procedure as the DDD simulation data.

Figures 8(a)–(c) show the misorientation along the torsion axis for a ⟨100⟩ oriented sample. The reference point for figure 8(a) is the bottom center. Line plots along the torsion axis are included in figure 8(b) and a local measure for the misorientation is depicted in figure 8(c), analog to the analysis of the simulation results in figure 2. The misorientation changes from the bottom to the top which is an expected natural outcome of torsion loading. The change in misorientation along the torsion axis in different cuts is almost linear, but there are small variations along individual lines corresponding to noise in the data. The local measure with a right-upper-neighbor misorientation shows traces of slip plane intersections.

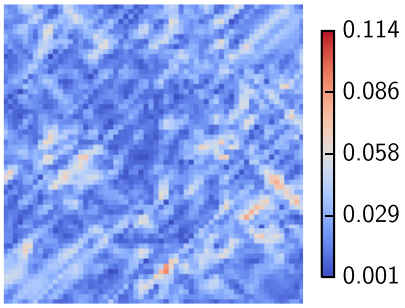


(a) ⟨100⟩ sample: Misorientation angle w.r.t. right upper neighbor cell.

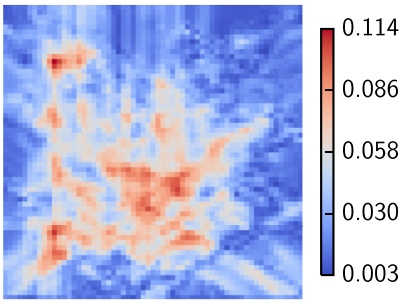


(b) ⟨111⟩ sample: Misorientation angle w.r.t. right neighbor cell.

**Figure 7.** Selective misorientation angles map for both torsion axes from DDD in a cross-section at height $y_{\max}/2$.

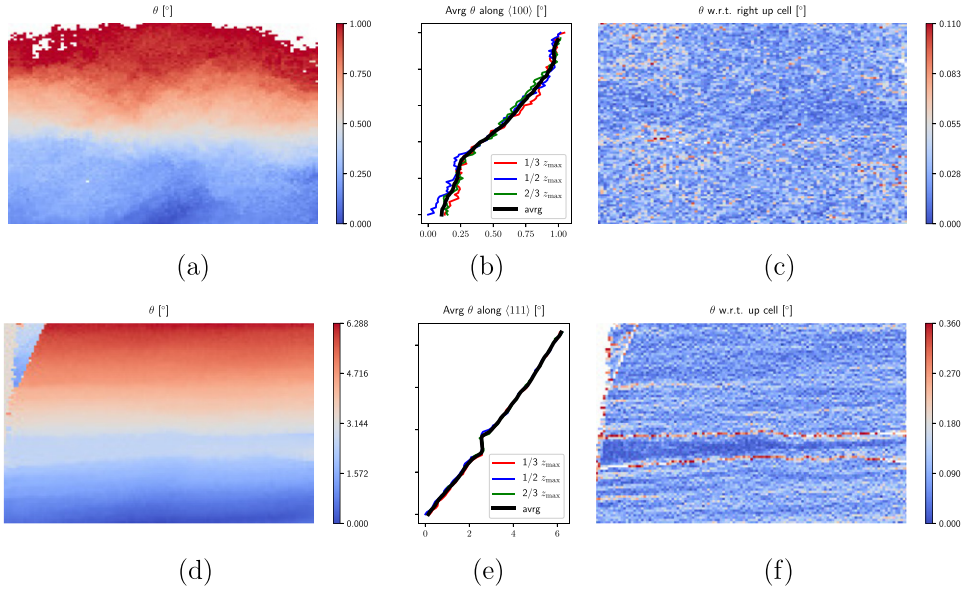


**Figure 8.** Misorientation maps of from experimental samples along the torsion axis of a ⟨100⟩-oriented grain in (a) to (c) and a ⟨111⟩ oriented grain in (d) to (f): (a) and (d) in-plane, reference bottom center; (b) and (e) misorientation along the torsion axis and lines parallel to it; (c) and (f) misorientation angle with respect to right upper neighbor.

Figures 8(d)–(f) show the misorientation along the torsion axis for a ⟨111⟩ oriented sample. The reference point for the global change is again the bottom center. Line plots along torsion axis directions are very much the same and there is no gradient orthogonal to the torsion axis direction, i.e. from the center to the sample surface (figure 8(e)). The local measure of misorientation shown in figure 8(f) is calculated with the upper neighbor and reveals distinct lines of

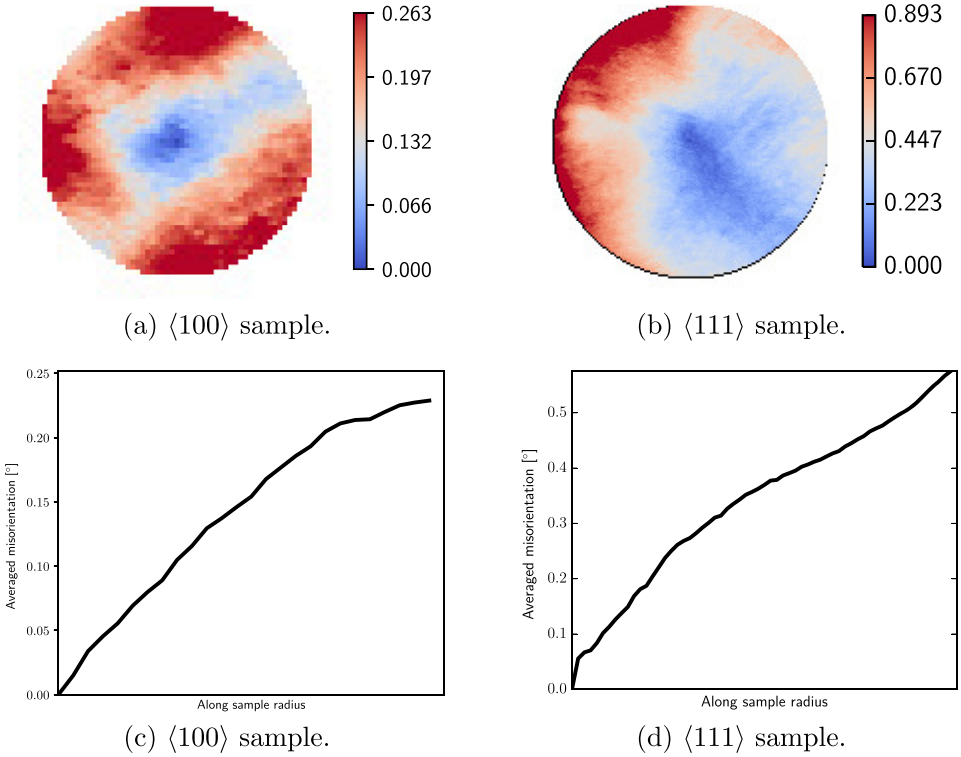


(a) ⟨100⟩ sample. (b) ⟨111⟩ sample.

(c) ⟨100⟩ sample. (d) ⟨111⟩ sample.

**Figure 9.** Misorientation maps of cross sections with respect to center from experiments (a) and (b). The same data set radially averaged in (c) and (d).

large misorientations, which lie almost parallel to each other and coincide with the slip plane orientation.

Figure 9 shows the misorientation of each data point with respect to the center pixel coinciding with the torsion axis for both orientations. Both data sets show a large variation of the misorientation in parts of the outer perimeter. This is due to a misalignment of the actual crystallographic orientation with respect to the perfect ⟨100⟩ or ⟨111⟩ orientation [8]. Both data sets exhibit a very small misorientation in the center region, which increases with increasing radius, more clearly visible in figures 9(c) and (d) which show the radially averaged misorientation versus radius. In contrast to [8], where the same analysis is done on a different wire, the data here does not level off towards the surface. This is attributed to the different grains which are examined with slightly different orientations and degree of deformation.

The selective KAM map of the ⟨100⟩ cross section (figure 10(a)) again shows individual lines of high misorientation angles which are spanning across the wire cross section. The lines are parallel to ⟨110⟩ directions of the crystal in case of the ⟨100⟩ oriented crystal.

In contrast, the selective KAM map of the ⟨111⟩ cross section (figure 10(b)) only shows line fragments at the outer circumference of the cross section. They are stronger at locations of higher overall misorientation where also edge effects of the sample preparation may influence the EBSD results.

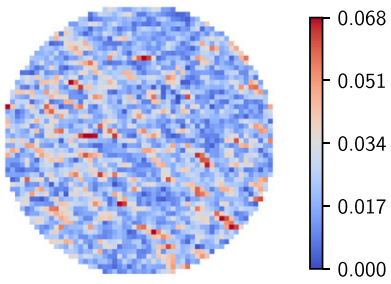


(a) ⟨100⟩ sample; misorientation w.r.t. right upper neighbor cell.

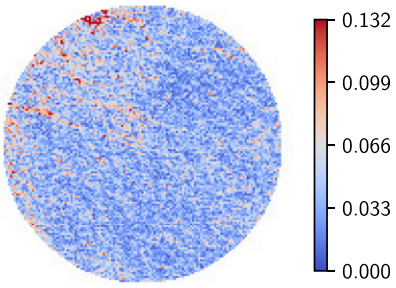


(b) ⟨111⟩ sample; misorientation w.r.t. right neighbor cell.

**Figure 10.** Selective misorientation maps for both torsion axes from experimental cross section. The step size has been varied for different EBSD scans to adapt for charging and drift during the measurement.

## 4. Discussion

From the surface traces observed in the DDD simulations of the ⟨100⟩ torsion axis specimen (cf figures 1(a) and 2(a)), it is clearly visible that dislocation glide is active on all primary slip planes. Visual microstructure analysis shows that dislocations move over the neutral axis, which is reflected by the diagonals present in misorientation maps with respect to the right upper neighbor (figure 2(d)). Experimental data from the cross section (figure 10(a)) also confirms homogeneous dislocation activity across the cross section and traces of intersections of slip planes with the cross section of the wire are visible. This leads to a finite plastic equivalent strain in the center of the wire as shown in figure 6. This can not be reproduced by classical crystal plasticity (CP) models or even strain gradient plasticity models [13]. Plasticity in those models is the result of locally exceeding the yield stress. With a neutral fiber like in torsion this condition can never be met. Interestingly, also the CDD result for thicker wires do not show a finite equivalent plastic strain in the center of the wire [31]. This again hints at the importance of the dislocation–dislocation interactions which *drive* dislocations across the neutral fiber resulting in a non-zero plastic strain (cf [14]). A possible reason for the absence of plastic strain in the central column might be the larger wire diameter and the lack of microstructural heterogeneity both reducing effectively pile-up like structures. Physically, the origin of the finite plastic strain spreading across the neutral axis in the DDD results is due to the dislocation interaction in pile-up like dislocation arrangements. In these pile-ups, dislocations starting from the outer region push inner dislocations over the neutral fiber as can be seen from resolved shear stress analysis for torsion loading, see e.g. [12, 14, 32]. Similar observations have been made for bending loading conditions [14, 21, 33].

The motion of dislocations across of the neutral fiber/plane is not a local phenomenon but representative for the whole sample as can be seen by the selective misorientation map with respect to the right upper neighbor of the DDD simulation in figure 7(a) additionally confirmed by the experimental data in figure 10(a). Dislocations moving across the neutral fiber in a strain gradient is the result of mutual repulsion [14].

In experiments slip traces can be observed which surround the whole sample. The emergence of the slip traces is attributed to the collective motion of dislocations on adjacent slip planes. In the limit of very low dislocation density an individual dislocation can pass the complete cross section without encountering other dislocations upon unloading, which was shown

in [14]. Here, dislocations will intersect with others due to the high dislocation density (*forest* interaction). This inhibits further motion and additionally stabilizes the structure upon unloading. Therefore other dislocations on the same or neighboring planes can still glide and form a visible step which involves effectively more than one slip plane. The 3D data of the dislocations in the DDD simulations supports this. The dislocation structure does not exhibit a substructure on single slip planes formed during loading but exhibit slip traces on the sample surface. Although the experimental resolution does not allow to distinguish between individual slip planes, the similarity in the overall/global deformation behavior can be explained unambiguously by the complementary approach. Further, the homogeneous activity of dislocations in the $\langle 100 \rangle$ case leads to the formation of substructures which effectively provide a twist around the torsion axis. E.g. the pattern of dislocations analyzed by selective misorientation in figure 7(a) shows a signature similar to the structure found in other DDD simulations [17]. The reason we do not see an explicit structure like in [17] can most probably be attributed to the much higher dislocation density used here. More dislocations might provide a twist without the formation of an explicit dislocation network. This is supported by the selective misorientation from figure 2(d) which shows rotations roughly around the axis of the inclined glide plane normals. Combining all rotations around all glide plane normals leads to an effective twist around the torsion axis shown in figure 2(b).

For the $\langle 111 \rangle$ specimen DDD and experiment show very good qualitative agreement: a strong localization on distinct slip planes orthogonal to the torsion axis is present in both cases (cf figures 2 and 8). This localization, again, can not be modeled with classical CP models, since the stress state is homogeneous along the sample. Regions of large misorientation in the experiment indicate a high dislocation density which is confirmed by the observation of dislocation structures from DDD simulations.

In more detail, the dislocation structure from the DDD simulation in figure 4 shows the formation of hexagonal networks of dislocations with screw character, a substructure naturally formed during torsion loading. This substructure is not an artifact of the square cross-section used here, but a result of the overall stress state and dislocation interactions as it is also observed by MD and other DDD simulations of small wires under torsion load [10, 11, 16, 34]. Specific substructures found at different distinct heights of the sample may be attributed to the local dislocation content and character, cf [15, 16]. Specifically the results in [16] show a heterogeneous distribution of dislocation activity which is not symmetric. The dislocation density in our samples is relatively high but plasticity is still a local phenomenon, therefore the network towards the sample corners is not an effect of top and bottom boundary conditions or the difference in cross-section shape, but of the crystallographic orientation, the initial dislocation structure, and torsion loading which then develops into the networks typically also observed by others.

Figure 11 gives the extent of this structure in 3D from DDD simulations. A relative misorientation for each voxel is calculated with respect to its surrounding 26 neighbors. For clarity of presentation, all misorientations smaller than $0.04^\circ$ are not shown. Regions of high misorientation correspond to regions where a hexagonal network of dislocations (figure 4) is formed on planes orthogonal to the torsion axis. This structure is not only formed, but is also the reason for orthogonal surface steps in the experiments (figure 1), further confirmed by the plastic strain contributions of slip systems extracted from DDD (figure 3(d)). Here, the B-systems clearly contribute the most to the plastic strain and therefore shear off the wire.

However, it cannot be stated in general that a high dislocation density comes with a high contribution to plastic strain. This can be rationalized by looking at the evolution of the dislocation density and equivalent strain contributions of the $\langle 100 \rangle$ orientation (figures 3(a) and (c)).

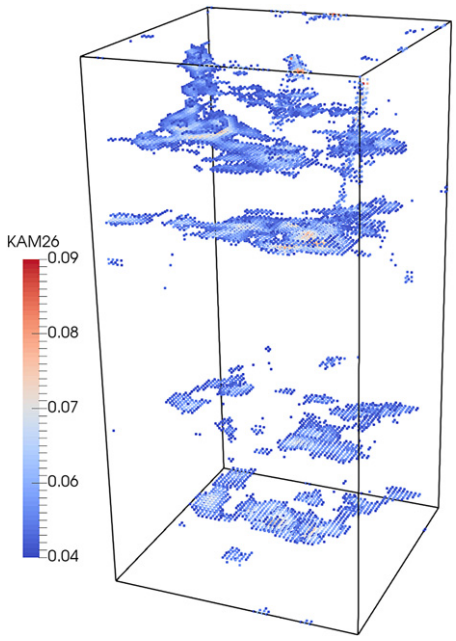


**Figure 11.** 3D rendering of the structure forming during torsion loading with a ⟨111⟩ axis. Voxels are colored according to KAM26 (misorientation with respect to all 26 neighbors of each voxel) misorientation analysis. Voxels with misorientations smaller than 0.04° are not shown.

Systems A3, B4, C3 and D4 show the largest increase in dislocation density but the largest contributions to the plastic strain are from systems B2, A3 and C3. Only two of the high dislocation density systems also have a large contribution to the plastic strain. A possible explanation is that not all dislocation density is produced by bow out, some is also produced (or annihilated) by deposition in a junction, e.g. glissile junctions, cross-slip, and annihilation [35]. Furthermore, a contribution to plastic strain does not necessarily imply dislocation storage: dislocations can also escape through the surfaces and leaving none or only very little dislocation density in the volume, while the contribution of the corresponding slip system to the plastic strain can be large. And by design of the current problem, the resolved shear stress close the sample surface (torsion loading and image forces) is the largest. The slip trace, which is visible on the sample surface, confirms this (figures 2(a) and (e)).

The explanation for the formation mechanism of the hexagonal structure is based on microstructural analysis: all dislocations on primary slip planes can in principle be activated since all experience a large enough resolved shear stress. In the torsion gradient dislocations on some slip systems orient themselves into mostly screw type dislocations. The resolved shear stress on the ⟨111⟩ plane orthogonal to the torsion axis is approximately 1.5–2 times larger than on the other ones. High activation and forest-type interactions lead to glissile junction formation and cross-slip in this plane. Due to their respective Burgers vectors (B-systems), they form a hexagonal network of screw dislocations (cf [36–38]). With cross-slip a dislocation first has to meet other dislocations to form a hexagon. The glissile junction already gives a partial hexagonal structure when formed. The formation of in-plane glissile junctions (two dislocations with different Burgers vectors produce a dislocation with the third one in the plane), facilitates the formation of the hexagonal arrangement. Strong collinear junctions

can be formed e.g. through further cross-slipping dislocations [39, 40], which stabilize this structure in the unloaded state. This network creates an effective visible slip step, which is not confined to exactly one slip plane, but extends over several planes through multiple glissile junctions and cross-slip events. The formed structure can be interpreted as a small angle twist boundary. This angle approximated using $\theta = b/D$, where $\theta$ is the misorientation angle, $b$ the magnitude of the Burgers vector and $D$ the mean dislocation spacing of the structure. The slice in figure 4 has a dislocation spacing of $D \approx 0.3$ $\mu$m and $b = 0.286$ nm, resulting in a misorientation angle of $\theta \approx 0.05°$. The corresponding misorientation values for the planar structure in the 3D KAM26 visualization in figure 11 are $\theta_{\mathrm{KAM26}} > 0.04°$ which confirms the interpretation of this dislocation structure as a small angle grain boundary.

Classical CP simulations can not capture the essentials of the observed features by design. Neither plasticity in the center nor the formation of a substructure or localization of slip can be modeled since plasticity in the context of CP is the consequence of exceeding the local yield stress. Furthermore microstructural features, such as the formation of patches of twist grain boundaries, as observed here, require dislocation–dislocation interactions. Even very advanced formulations like the CDD framework do not exhibit the essential observations of our results [31]. While the CP modeling in general might be the correct approach for larger samples, we use the comparison here to strongly advocate for different and microstructure based models in the given size regime.

Even though the employed methods are different in nature with different shortcomings (alignment of the sample in experiments, square cross section in DDD, size differences, different material systems, polycrystalline vs single crystal sample, loaded vs unloaded, etc), we show that it is possible to fuse the data from both methods to understand dislocation substructure formation and explain deformation modes. This is achieved by using the measure of local misorientations. It is independent of the exact crystallographic features like lattice constant and Burgers vector and provides a common language for comparison. No stresses are compared directly and if, this could—at least partially—be accounted for by normalization to e.g. the shear modulus and the Burgers vector, as is often done.

The explanation for the formation of the substructure in the $\langle 111 \rangle$ case is based on glissile junctions and cross-slip. Both occur equally often in the presented DDD simulations. A high probability for the formation of glissile junctions is given by the high dislocation density and the sample size and the activation of almost all slip systems [41]. It is a geometrical operation, which is independent of the specific fcc material. Cross-slip into the B system of the $\langle 111 \rangle$ sample is favored because of the 1.5–2 times higher resolved shear stress than on the inclined planes. A lower cross-slip probability (for a different specific fcc material Al vs Au) can be counteracted by high local stresses due to dislocation–dislocation interaction and surface image forces, which have been reported to increase cross-slip probability [42]. We further note that MD simulations of torsion for small nanowires have been reported for both Al and Au and while the specific dislocation arrangement differs—mainly due to the different partial dislocation separation distances based on the difference in stacking fault energy—the arrangements are qualitatively very close: both materials show a network of screw dislocations [11]. In short, the formation of the substructure depends on forest hit rate, given by sample size and dislocation density, favorable higher shear stress in the B plane and local high stresses. A different specific material choice would probably change the individual weighting of the contributions, but it is not expected to change the overall picture.

## 5. Conclusion

We successfully use a combination of small scale experiments on bamboo-structured microwires with single crystalline DDD simulations to understand deformation mechanisms in torsion loading for two torsion axes. By calculating the misorientation caused by dislocations in the DDD simulations, a link to the experiments is established, which allows for an explanation of experimentally observed misorientation patterns and formation of circumferential surface traces.

Experimentally observed surface traces in $\langle 100 \rangle$ grains are the result of the motion of dislocations on close-by parallel slip planes generating an effective slip trace on the surface. The dislocation structure on these slices leads to inclined gradients in the misorientation analysis shown in figures 2(d) and 8(c). Based on the analysis of misorientations of the cross section along and perpendicular to the torsion axis we suggest that the homogeneous activation of dislocations on all slip planes provides individual twist components around the glide plane normals which *effectively* results in a global twist around the torsion axis. A clarification of dislocation structure formation on inclined planes requires further analysis which is part of future work.

The surface traces observed in the $\langle 111 \rangle$ case (figures 1(b) and 4) are the result of glissile junctions and cross-slipping dislocations into this plane. Slip systems in this plane contribute the most to the plastic strain, because the Schmid factor in this plane is the highest. The dislocations form hexagonal networks via collinear and glissile junctions which stabilize the structure during unloading. The interpretation of this structure as a small angle twist boundary is clearly justified and experimental data shows corresponding signatures.

None of these features can be modeled with classical CP simulations, showing the limits of this type of approach in this size regime: all plasticity is homogeneous and only dependent on the local stress. No plasticity will be found in the neutral fiber in the center, where DDD simulations and experiments show plasticity. This plasticity is caused by dislocations in pile-up like arrangement in the gradient, which are pushed across the neutral fiber.

## Acknowledgments

This work was performed on the computational resource bwUniCluster funded by the Ministry of Science, Research and Arts and the Universities of the State of Baden-Württemberg, Germany, within the framework program bwHPC. The financial support for the research group FOR1650 *Dislocation based plasticity* funded by the German Research Foundation (DFG) under contract numbers WE3544/5-2 and GR3677/2-2 is gratefully acknowledged by MS, DW and MZ, PG, MW respectively. The authors gratefully acknowledge the Open Access fund of the Ruhr-Universität Bochum.

## Data availability statement

The data that support the findings of this study are available upon reasonable request from the authors.

## Appendix A. Displacement fields for a given dislocations microstructure

The calculation of the displacement field at any position is described in the reference paper [22]. The three dimensional implementation of the superposition approach [24] requires the

displacement fields to allow for a mechanical consistent boundary value problem using the small strain assumption. The calculation is based on corrected displacement fields of triangular dislocation loops [43, 44]. The displacement field calculation is decomposed into two contributions: (i) a term which contains only the Burgers vector $\vec{b}$ and the solid angle $\Omega$ which the triangular loops spans with the evaluation position $r$ and (ii) a term which contains the contribution depending on the elastic properties. The solid angle term (i) changes sign and jumps by $\vec{b}$, when evaluating the displacement along a line crossing the area swept by the dislocation line.

In the framework a dislocation loop is always planar. A dislocation is represented by a sequence of connected straight segments. Therefore the dislocation loop is readily decomposed into triangular dislocation loops. The swept area of each dislocation loop [22, 25] is tracked. Junction formation (Lomer, glissile, cross-slip, Hirth) leads to superposition of segments at the junctions and shared nodes. The junction may then have effectively a zero Burgers vector, e.g. in case of cross-slip or glissile junction, where a third loop used to represent the glissile dislocation [25, 41]. Thus individual loops remain closed within their slip plane. The total displacement due to a given dislocation structure can be evaluated at any point $r$ within the volume in a post-processing operation. A cut-off procedure is used for distances smaller than $b$ to the dislocation core which sets the resolution limit for this contribution.

For sake of computational efficiency only those sides of the triangular dislocation loops which coincide with actual dislocation segments require the calculation of the complete expression. For those sides of the triangular loops present due to the decomposition only, the evaluation of the solid angle expression calculation is sufficient. This contribution contains the slip discontinuity. Instead of using the solid angle calculation proposed in [43], a numerically more efficient term proposed in [45] is used and adapted to the sign conventions used here. This term requires the evaluation of one atan2$(y, x)$ function only and is therefore approximately three times faster.

A second contribution to the displacement field of the dislocation is due to the correction fields from the boundary value problem which allows to describe finite sized samples. The accuracy of the contribution depends on the resolution of the FEM mesh used, but the overall fields are smooth within the volume. As shown for the image stresses and traction cancellation [22], the error on the nodal image force of a segment piercing through the first element is significant ($\approx 10\%$) even for regularized stress fields and the same holds for the displacement fields. Therefore we are confident, that the overall trends are representative for the considered scenario.

The evaluation of the rotation due to the current dislocation structure requires the knowledge of the displacement gradient (distorsion) within the volume. Here we are considering only the displacement gradient caused by the dislocation configuration. Therefore only the displacement contribution of the dislocations including the image contribution of the elasticity problem have to be extracted. To do so, two boundary value problems are solved. The surface areas having displacement respective traction free boundary conditions are denoted $S_\mathrm{u}$ and $S_\mathrm{t}$.

- The normal DDD superposition problem is solved: the boundary conditions for dof on $S_\mathrm{u}$ are $\hat{u}_\mathrm{I} = u_\mathrm{tot} - \tilde{u}$, where $\tilde{u}_\mathrm{tot}$ are the total imposed displacements, $\tilde{u}$ are the displacement fields from all dislocation calculated in infinity space resulting in $\hat{u}_\mathrm{I}$. For the dofs belonging to $S_\mathrm{t}$, traction free boundary conditions are applied with $\hat{\sigma} = -\tilde{\sigma}$, where $\tilde{\sigma}$ are the stress fields of all dislocations.
- A second elastic problem using the imposed displacement (torsion) on $S_\mathrm{u}$ and traction free boundary conditions on $S_\mathrm{t}$ expressed by $\hat{u}_\mathrm{II} = u_\mathrm{tot}$ and $\hat{\sigma} = 0$.

The plastic displacement field is then obtained as $u = \hat{u}_\mathrm{I} - \hat{u}_\mathrm{II}$.

The plastic displacement gradient is derived from the total dislocations displacement fields $u$. In order to properly take into account the displacement jumps due to the singular solid angle term, the evaluation is performed loop wise. The displacement gradient is evaluated by a simple finite difference scheme. Each time the line drawn between the evaluation points required for the finite difference scheme cross the area swept/encircled by the dislocation the resulting finite difference is corrected for the corresponding jump. Thus no artificial rotation is introduced by the discontinuous displacement field. The numerically determined plastic displacement gradients contributions $\partial \tilde{u}_i / \partial x_j$ for dislocation loops were validated against an analytical solution for segments obtained using Mathematica.

### *A.1. Calculation of misorientation from distorsion field*

The relationship between the distortion and the infinitesimal rotation tensor reads

$$W_{ij} = \frac{1}{2}\left(\frac{\mathrm{d}u_i}{\mathrm{d}x_j} - \frac{\mathrm{d}u_j}{\mathrm{d}x_i}\right). \tag{A.1}$$

It has three independent components and it can therefore be written as a product of an angle and a (normed) rotation axis $\mathbf{w} = \alpha\mathbf{n}$, where $\alpha$ is the rotation angle and $\mathbf{n}$ the rotation axis. The relationship between the components is

$$\mathbf{W} = \begin{bmatrix} 0 & -w_3 & w_2 \\ w_3 & 0 & -w_1 \\ -w_2 & w_1 & 0 \end{bmatrix} \leftrightarrow \mathbf{w} = \begin{bmatrix} w_1 \\ w_2 \\ w_3 \end{bmatrix}. \tag{A.2}$$

From the rotation angle and axis, a rotation matrix can be constructed:

$$\mathbf{R} = \cos(\alpha)\,1 + (1 - \cos(\alpha))(\mathbf{n} \otimes \mathbf{n}) + \sin(\alpha) \begin{bmatrix} 0 & -n_3 & n_2 \\ n_3 & 0 & -n_1 \\ -n_2 & n_1 & 0 \end{bmatrix}. \tag{A.3}$$

The rotation matrix $\mathbf{R}$ is evaluated at each site and used for the computation on the misorientation with respect to a reference. In the following, $\mathbf{R}_{\mathrm{ref}}$ refers to the rotation matrix of the reference pixel and $\mathbf{R}$ to any pixel whose misorientation is to be calculated with respect to that reference. The orientation relationship and the angle $\theta$ between two sites is described by:

$$\mathbf{R}_{\mathrm{mis}} = \mathbf{R}_{\mathrm{ref}}\mathbf{R}^{-1}, \tag{A.4}$$

$$\theta = \mathrm{acos}\left(\frac{\mathrm{tr}\,(\mathbf{R}_{\mathrm{mis}}) - 1}{2}\right). \tag{A.5}$$

The KAM with eight neighbors averages this measure of one voxel with the surrounding 8. KAM26 respectively averages 26 neighbors in three dimensions. Average misorientation with respect to right upper neighbor is this measure where $\mathbf{R}$ is the $\mathbf{R}_{\mathrm{ref}}$ right upper neighbor with respect to its position as depicted in the figures.

## ORCID iDs

Markus Stricker https://orcid.org/0000-0002-8933-0238
Daniel Weygand https://orcid.org/0000-0002-8681-3904

## References


[1] Dehm G, Motz C, Scheu C, Clemens H, Mayrhofer P H and Mitterer C 2006 Mechanical size-effects in miniaturized and bulk materials *Adv. Eng. Mater.* **8** 1033–45

[2] Kraft O, Gruber P A, Mönig R and Weygand D 2010 Plasticity in confined dimensions *Annu. Rev. Mater. Res.* **40** 293–317

[3] Idiart M I and Fleck N A 2010 Size effects in the torsion of thin metal wires *Modelling Simul. Mater. Sci. Eng.* **18** 015009

[4] El-Awady J A 2015 Unravelling the physics of size-dependent dislocation-mediated plasticity *Nat. Commun.* **6** 5926

[5] Kiener D, Grosinger W, Dehm G and Pippan R 2008 A further step towards an understanding of size-dependent crystal plasticity: *in situ* tension experiments of miniaturized single-crystal copper samples *Acta Mater.* **56** 580–92

[6] Imrich P J, Kirchlechner C, Motz C and Dehm G 2014 Differences in deformation behavior of bicrystalline Cu micropillars containing a twin boundary or a large-angle grain boundary *Acta Mater.* **73** 240–50

[7] Chen Y, Kraft O and Walter M 2015 Size effects in thin coarse-grained gold microwires under tensile and torsional loading *Acta Mater.* **87** 78–85

[8] Ziemann M *et al* 2015 Deformation patterns in cross-sections of twisted bamboo-structured Au microwires *Acta Mater.* **97** 216–22

[9] Fleck N A, Muller G M, Ashby M F and Hutchinson J W 1994 Strain gradient plasticity: theory and experiment *Acta Metall. Mater.* **42** 475–87

[10] Weinberger C R and Cai W 2010 Plasticity of metal wires in torsion: molecular dynamics and dislocation dynamics simulations *J. Mech. Phys. Solids* **58** 1011–25

[11] Weinberger C R and Cai W 2010 Orientation-dependent plasticity in metal nanowires under torsion: twist boundary formation and Eshelby twist *Nano Lett.* **10** 139–42 PMID: 20030357

[12] Senger J, Weygand D, Kraft O and Gumbsch P 2011 Dislocation microstructure evolution in cyclically twisted microsamples: a discrete dislocation dynamics simulation *Modelling Simul. Mater. Sci. Eng.* **19** 074004

[13] Bayerschen E, Prahs A, Wulfinghoff S, Ziemann M, Gruber P A, Walter M and Böhlke T 2016 Modeling contrary size effects of tensile- and torsion-loaded oligocrystalline gold microwires *J. Mater. Sci.* **51** 7451–70

[14] Stricker M, Weygand D and Gumbsch P 2017 Irreversibility of dislocation motion under cyclic loading due to strain gradients *Scr. Mater.* **129** 69–73

[15] Ryu I, Gravell J D, Cai W, Nix W D and Gao H 2020 Intrinsic size dependent plasticity in BCC micro-pillars under uniaxial tension and pure torsion *Extreme Mech. Lett.* **40** 100901

[16] Ryu I, Cai W, Nix W and Gao H 2016 Anisotropic size-dependent plasticity in face-centered cubic micropillars under torsion *JOM* **68** 253–60

[17] Gravell J D, Lee S, Ryu S and Ryu I 2021 Effect of size and orientation on stability of dislocation networks upon torsion loading and unloading in FCC metallic micropillars *Acta Mater.* **214** 117010

[18] Dunstan D J and Bushby A J 2014 Grain size dependence of the strength of metals: the Hall–Petch effect does not scale as the inverse square root of grain size *Int. J. Plast.* **53** 56–65

[19] Liu D, He Y, Tang X, Ding H, Hu P and Cao P 2012 Size effects in the torsion of microscale copper wires: experiment and analysis *Scr. Mater.* **66** 406–9

[20] Yang B, Motz C, Rester M and Dehm G 2012 Yield stress influenced by the ratio of wire diameter to grain size—a competition between the effects of specimen microstructure and dimension in micro-sized polycrystalline copper wires *Phil. Mag.* **92** 3243–56

[21] Motz C, Weygand D, Senger J and Gumbsch P 2008 Micro-bending tests: a comparison between three-dimensional discrete dislocation dynamics simulations and experiments *Acta Mater.* **56** 1942–55

[22] Weygand D, Friedman L H, der Giessen E V and Needleman A 2002 Aspects of boundary-value problem solutions with three-dimensional dislocation dynamics *Modelling Simul. Mater. Sci. Eng.* **10** 437–68

[23] Senger J, Weygand D, Gumbsch P and Kraft O 2008 Discrete dislocation simulations of the plasticity of micro-pillars under uniaxial loading *Scr. Mater.* **58** 587–90

[24] der Giessen E V and Needleman A 1995 Discrete dislocation plasticity: a simple planar model *Modelling Simul. Mater. Sci. Eng.* **3** 689–735

[25] Weygand D and Gumbsch P 2005 Study of dislocation reactions and rearrangements under different loading conditions *Mater. Sci. Eng.* A **400–401** 158–61
[26] Weygand D, Senger J, Motz C, Augustin W, Heuveline V and Gumbsch P 2009 High performance computing and discrete dislocation dynamics: plasticity of micrometer sized specimens *High Performance Computing in Science and Engineering' 08* eds Wolfgang E Nagel, Dietmar B Kröner and Michael M Resch (Berlin: Springer) pp 507–23
[27] Zaiser M and Sandfeld S 2014 Scaling properties of dislocation simulations in the similitude regime *Modelling Simul. Mater. Sci. Eng.* **22** 065012
[28] Walter M and Kraft O 2011 A new method to measure torsion moments on small-scaled specimens *Rev. Sci. Instrum.* **82** 035109
[29] Walter M D, Kraft O P D and Klotz M 2011 *Device for determining torsional moments in the submicron Newton metre range* European Union EP 1903326 B1 available from: https://patents.google.com/patent/EP1903326B1/en
[30] Wilkinson A J 2001 A new method for determining small misorientations from electron back scatter diffraction patterns *Scr. Mater.* **44** 2379–85
[31] Zoller K and Schulz K 2020 Analysis of single crystalline microwires under torsion using a dislocation-based continuum formulation *Acta Mater.* **191** 198–210
[32] Jones R E, Zimmerman J A and Po G 2016 Comparison of dislocation density tensor fields derived from discrete dislocation dynamics and crystal plasticity simulations of torsion *J. Med. Sci. Res.* **5** 44–62
[33] Cleveringa H H M, der Giessen E V and Needleman A 1999 A discrete dislocation analysis of bending *Int. J. Plast.* **15** 837–68
[34] Weinberger C R and Cai W 2012 Plasticity of metal nanowires *J. Mater. Chem.* **22** 3277–92
[35] Stricker M, Sudmanns M, Schulz K, Hochrainer T and Weygand D 2018 Dislocation multiplication in stage II deformation of fcc multi-slip single crystals *J. Mech. Phys. Solids* **119** 319–33
[36] Gwinner D and Packeiser G 1980 Dislocation networks in twisted silicon *Phil. Mag.* A **42** 645–60
[37] Packeiser G and Gwinner D 1980 The formation mechanisms of dislocation networks in twisted silicon *Phil. Mag.* A **42** 661–70
[38] McClintock F A and Prinz F 1983 A model for the evolution of a twist dislocation network *Acta Metall.* **31** 827–32
[39] Madec R, Devincre B, Kubin L, Hoc T and Rodney D 2003 The role of collinear interaction in dislocation-induced hardening *Science* **301** 1879–82
[40] Devincre B, Hoc T and Kubin L P 2005 Collinear interactions of dislocations and slip systems *Mater. Sci. Eng.* A **400–401** 182–5
[41] Stricker M and Weygand D 2015 Dislocation multiplication mechanisms—glissile junctions and their role on the plastic deformation at the microscale *Acta Mater.* **99** 130–9
[42] Hussein A M, Rao S I, Uchic M D, Dimiduk D M and El-Awady J A 2015 Microstructurally based cross-slip mechanisms and their effects on dislocation microstructure evolution in fcc crystals *Acta Mater.* **85** 180–90
[43] Barnett D M 1985 The displacement field of a triangular dislocation loop *Phil. Mag.* A **51** 383–7
[44] Barnett D M and Balluffi R W 2007 The displacement field of a triangular dislocation loop—a correction with commentary *Phil. Mag. Lett.* **87** 943–4
[45] Van Oosterom A and Strackee J 1983 The solid angle of a plane triangle *IEEE Trans. Biomed. Eng.* **BME-30** 125–6